Available online at www.sciencedirect.com
SCIENCE DIRECT®
Acta Materialia 52 (2004) 4413–4425
Acta MATERIALIA
www.actamat-journals.com

Computational description of nanocrystalline deformation based on crystal plasticity

Hsueh-Hung Fu, David J. Benson, Marc André Meyers *

Department of Mechanical and Aerospace Engineering, University of California, San Diego, Mail Code 0411, La Jolla, CA 92093, USA

Received 22 January 2004; received in revised form 20 May 2004; accepted 21 May 2004
Available online 20 July 2004

Abstract

The effect of grain size on the mechanical response of polycrystalline metals was investigated computationally and applied to the nanocrystalline domain. A phenomenological constitutive description is adopted to build the computational crystal model. Two approaches are implemented. In the first, the material is envisaged as a composite; the grain interior is modeled as a monocrystalline core surrounded by a mantle (grain boundary) with a lower yield stress and higher work hardening rate response. Both a quasi-isotropic and crystal plasticity approaches are used to simulate the grain interiors. The grain boundary is modeled either by an isotropic Voce equation (Model I) or by crystal plasticity (Model II). Elastic and plastic anisotropy are incorporated into this simulation. An implicit Eulerian finite element formulation with von Mises plasticity or rate dependent crystal plasticity is used to study the nonuniform deformation and localized plastic flow. The computational predictions are compared with the experimentally determined mechanical response of copper with grain sizes of 1 μm and 26 nm. Shear localization is observed during work hardening in view of the inhomogeneous mechanical response. In the second approach, the use of a continuous change in mechanical response, expressed by the magnitude of the maximum shear stress orientation gradient, is introduced. It is shown that the magnitude of the gradient is directly dependent on grain size. This gradient term is inserted into a constitutive equation that predicts the local stress–strain evolution.

Keywords: Nanocrystalline materials; Grain size

1. Introduction

The mechanical behavior of nanocrystalline metals has been the object of recent intense study [1,2]. Experimental, analytical, and computational investigations are revealing the detailed mechanisms of plastic deformation. A universal observation is that the Hall–Petch slope shows a significant decrease as the grain size is decreased beyond 1 μm level (e.g. [2]).

1.1. Plasticity of crystals

The early study of single crystal deformation can be traced back to the experiments by Taylor and Elam [3]. A simplified polycrystal model was proposed by Taylor [4], who assumed that each grain in the crystalline aggregate was subjected to the same average strain as the whole matrix. This model has been widely adopted in the study of large deformation of polycrystals (e.g., Bishop and Hill [5], Bishop [6], Dillamore and Kaoth [7], and others). Hill and Rice [8] used an elastic–plastic rate-independent model to describe the behavior of crystal deformation. Asaro and Rice [9] found, in single slip deformation, that localized shear slip occurs as the plastic hardening modulus for this slip system approaches a small critical positive value. Thus, they proposed a constitutive model incorporating a deviation from the Schmid law.

Another approach to the finite strain of polycrystals is the development of self consistent models. The early work was done by Kröner [10] and Budianski and Wu [11]. This was followed by Berveiller and Zaoui [12] and

* Corresponding author. Tel.: +1-858-534-4719; fax: +1-858-534-5698.
E-mail address: mameyers@ucsd.edu (M. André Meyers).

1359-6454/$30.00 © 2004 Acta Materialia Inc. Published by Elsevier Ltd. All rights reserved.
doi:10.1016/j.actamat.2004.05.036

Molinari and coworkers [13,14]. Additional work on the constitutive description of crystal plasticity focused on experiment-based refinement and on incorporating the temperature effect. Recently, the entire subject was reviewed by Lubarda [15].

Texture evolution has been successfully modeled and correctly reproduces experimental results. Lin and Havner [16] modeled the texture evolution in an FCC crystal through rotations in an inverse pole figure. For instance, Anand and Kalidindi [17] applied the crystal plasticity formalism to predict earing in deep drawing operations and compared their computed textures with experimentally observed ones. The subject is comprehensively treated by Kocks et al. [18].

Beside the aforementioned research, numerical simulation provides another powerful means of exploring the material behavior and the interaction of polycrystals.

Peirce et al. [19,20] used a planar double slip model with viscoplasticity to simulate the nonuniform stress localization of a single crystal plate under tension (finite element method). Two slip systems are involved in a state of plane strain, since the third strain component is zero. Later, an idealized polycrystal model was introduced to investigate the intercrystal stress and texture evolution by Harren and Asaro [21]. Recently, the numerical research of polycrystal plasticity has migrated toward three-dimensional modeling, e.g. [22,23]. Barbe et al. [24] built a three-dimensional microstructure with Voronoi tesselation, but the simulation is limited to strains smaller than 0.002.

1.2. Grain-size effects

All the aforementioned models fail to predict a grain-size dependence of yield stress and work hardening. This is due to the fact that the problem is self-similar. Unless a scaling or gradient parameter is introduced, there can be no grain size dependence. Thus, the prediction of yield stress and work hardening as a function of grain size has escaped the reach of computational models. This is indeed surprising, since these models are rather complex and claim to predict polycrystalline behavior quantitatively. The effect of grain size on the yield stress can be brutal, as shown by Armstrong [25]. For instance the yield point of copper increases from approximately 25 to 135 MPa when the grain size is reduced from 1 mm to 1 μm.

The difficulty in predicting grain-size effects arises from the differences in physical processes occurring within the grain-boundary region and grain interiors. Ashby [26] postulated geometrically necessary dislocations to account for the inherent difference in the accumulation of plastic strain between the grain-boundary region and grain interior. He described the deformation of grain interiors as being primarily by single slip; in contrast, in both sides of the grain boundary, the lattice undergoes severe rotations, triggering secondary slip. Therefore, the work-hardening rate of regions adjoining the grain boundary is higher than in the grain interiors. Yao and Wagoner [27] carried out systematic experiments on aluminum multicrystals and quantitatively established the relative importance of different nucleation sites for slip. For the 84 slip bands observed, 43% nucleated at grain boundaries and only 13% at grain centers. Since the specimens contained from only 1 to 6 grains, a large fraction of the bands initiated at the specimen edges or in undefined locations (37%). These results confirm the importance of *grain boundaries as sources of slip*. Similar results were obtained, albeit without quantitative estimates, by Suits and Chalmers [28], Worthington and Smith [29], and Hook and Hirth [30]. Delaire et al. [31] performed tensile experiments on a copper multicrystal and demonstrated that there is a much greater tendency for slip in two or three systems in regions close to boundaries. In addition to the aforementioned effects, there are two factors contributing to the differences:

(a) The ease of dislocation nucleation at grain boundaries is accentuated; this may result in a lower yield stress.
(b) The maximum shear stress direction changes close to the grain boundary, because of elastic anisotropy. This factor was considered by Meyers and Ashworth [32].

Fig. 1 shows, in a schematic fashion, the effect of a grain boundary on evolution of plastic deformation. Far from

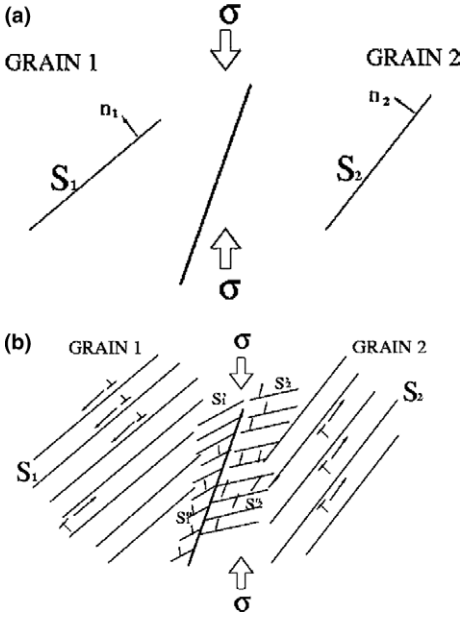

Fig. 1. (a) Two adjacent grains having slip systems S_1 and S_2 activated by imposed compressive tractions. (b) Slip systems S_1 (interior of Grain 1) and S_2 (interior of Grain 2) active far from boundary. Slip systems activated in grain-boundary vicinity: S_1', S_1'', and S_1 in Grain 1 and S_2', S_2'', and S_2 in Grain 2.

the boundary (the grain-interior region) and assuming single slip in both grains, slip system S_1 is activated in Grain 1, whereas slip system S_2 is activated in Grain 2; see Fig. 1(a). These are the systems having the highest resolved shear stress in the respective grains. In the vicinity of the grain boundary, the resolved shear stress orientation is altered due to elastic anisotropy constraints. This leads to the activation of sources in/adjacent to the grain boundary and slip in systems S_1' in Grain 1 and S_2' in Grain 2. The rotation of the angle of maximum shear stress with the loading axis leads to cross-slip; this is schematically shown by systems S_1'' and S_2'' in Grains 1 and 2, respectively. The net result is that this region hardens at a higher rate than the grain interiors.

There are efforts at incorporating this gradient work hardening into a computational framework. Fu et al. [33–35] introduced a discrete layer along the grain boundary with a high flow stress and low work hardening. In the first approach [33,34], an ideal plastic response was assumed in the grain-boundary region. This was later [35] rendered more physically significant by using a high work-hardening rate and a saturation stress (Voce equation). The yield stress of the grain-boundary layer is lower than that of the grain interior. Kim et al. [36] modeled the plastic deformation of nanocrystalline metals by constitutive equations based on dislocation density evolution and including a contribution from diffusion controlled plastic flow. Estrin et al. [37] proposed a crystal plasticity model including gradient terms for a double slip geometry. Diffusion-like second derivative terms were incorporated to account for dislocation cross-slip. Van Swygenhofen and coworkers [38,39] applied MD simulations to nanocrystalline materials and demonstrated that grain boundaries can accommodate strain by sliding and emission of partial dislocations.

In this paper, the model proposed by Fu et al. [33–35] is developed further. The ease of dislocation generation at the grain boundaries is represented in a novel manner by considering the grain-boundary region as having a yield stress lower than the grain interior. Crystal plasticity is introduced to treat the evolution of mechanical strength in a more realistic manner. These past models [33–35] use two discrete layers (core and mantle approximation). This was only a first model, and did not incorporate two important effects: (a) the slip and rotation of the lattice, and (b) the concept of rapid work hardening in the grain-boundary region. This is the primary goal of this report. Single crystal viscoplasticity is used, incorporating the combined effects of grain boundaries and grain interiors to provide a novel viewpoint. The approach introduced by Fu et al. [33–35] is now generalized by treating grains as individual single crystals, with defined slip systems. The scaling parameter introduced is the grain-boundary layer, which varies in a non-linear way with grain size. Thus, a continuous hardening model is introduced, which is computationally more complex. It is based on the change in orientation of the angle of maximum shear stress throughout the polycrystalline aggregate, which can be directly related to the work hardening. This gradient term is grain-size dependent.

2. Kinematics of crystal deformation and constitutive description

The isothermal, rate-dependent crystal plasticity model is introduced below. The kinematic basis for the material deformation is shown in Fig. 2(a). The deformation gradient of the material is decomposed into two parts (multiplicative decomposition by Lee and Liu [40]):

(a) *Plastic deformation:* Plastic flow through the lattice due to dislocation motion.
(b) *Non-plastic component:* Elastic deformation and rigid-body rotation of the lattice with material embedded in it.

According to the above decomposition, the deformation gradient F can be expressed as

$$F = F^* \cdot F^{\mathrm{P}}, \tag{1}$$

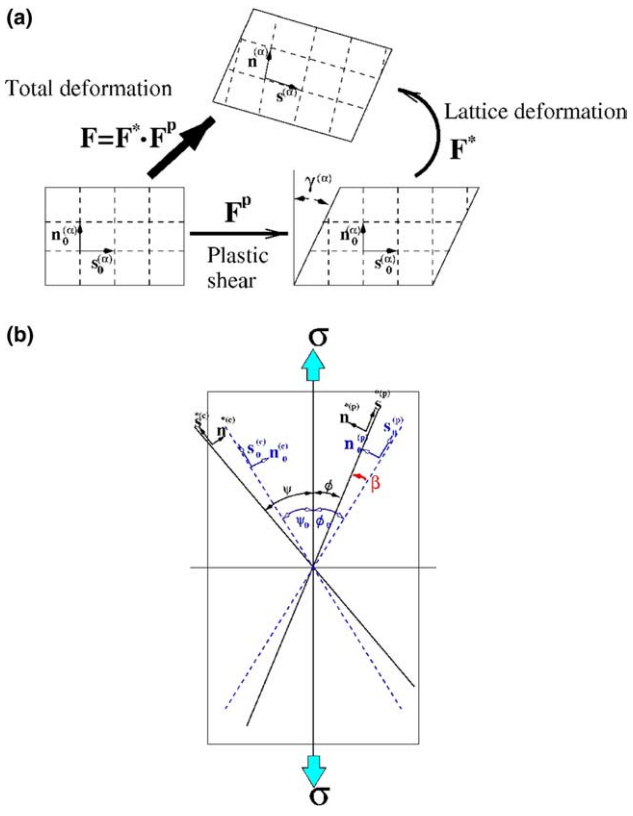

Fig. 2. (a) Decomposition of the total deformation gradient. (b) Planar double slip system of single crystal metal specimen under tension.

where F^{P} is the deformation gradient from crystallographic slip and $F^{*} = V^{\mathrm{e}}R^{*}$ accounts for the non-plastic part (including elastic stretching and the rigid body rotation of the lattice). The initial lattice vectors of an active slip system α, the slip plane normal n and the slip directions, are stretched and rotated with the lattice as (Fig. 2(b))

$$s^{(\alpha)} = F^{*} \cdot s_0^{(\alpha)}, \tag{2}$$

$$n^{(\alpha)} = n_0^{(\alpha)} \cdot F^{*-1}. \tag{3}$$

In the-rate dependent formulation, the slip evolution is not described by the loading condition as assumed in rate-independent models [41]. Instead, the visco-plastic slip system is described by a power relationship between stress and strain rate. A successful expression is the power relationship used by Hutchinson [42] for a slip system α; it has the form

$$\tau^{(\alpha)} = g^{(\alpha)} \left(\frac{\dot{\gamma}^{(\alpha)}}{\dot{a}} \right)^{m} \operatorname{sgn}\left(\frac{\tau^{(\alpha)}}{g^{(\alpha)}} \right), \tag{4}$$

where $\dot{a}$ is the reference slip rate, m is the rate sensitivity parameter, (the limit of $m \to 0$ is the rate independent case). The current slip resistance on the system α is $g^{(\alpha)}$ and the resistance of this slip system is initially the critical resolved shear stress. The following evolution equation for the current strain hardening state $g^{(\alpha)}$ can be used:

$$g^{(\alpha)} = \sum_{\alpha=1}^{n} h_{\alpha\beta} \dot{\gamma}^{(\beta)}. \tag{5}$$

Eq. (5) represents the orientation effect on slip system α for plastic slip to occur. The hardening matrix $h_{\alpha\beta}$ adopted by Hutchison [42] and Peirce et al. [19,20] is

$$h_{\alpha\beta} = [q + (1-q)\delta_{\alpha\beta}]h(\gamma), \tag{6}$$

where the q is the ratio of latent hardening to self-hardening rates. Its value is estimated to be between 1 and 1.4 from the experimental data [44], and

$$h(\gamma) = h_0 \operatorname{sec} h\left[\frac{h_0 \gamma}{\tau_{\mathrm{s}} - \tau_0} \right], \tag{7}$$

where h_0 is the initial hardening modulus and τ_{s} is the saturated shear strength. Eq. (7) is based on the single slip law, which comes from the approximation of experimental data

$$\tau(\gamma) = \tau_0 + (\tau_{\mathrm{s}} - \tau_0) \tanh\left(\frac{h_0 \gamma}{\tau_{\mathrm{s}} - \tau_0} \right), \tag{8}$$

where the $\tau(\gamma)$ is the current value of the flow stress in single slip. Extending the application of Eq. (8) to the multi-slip case, γ is defined as the cumulative shear strain on all slip systems, which is defined as

$$\gamma = \sum_{\alpha=1}^{n} |\gamma^{(\alpha)}|. \tag{9}$$

3. Results and discussion

Three models were used to treat the problem. They represent increasing departures from the earlier Fu et al. [33–35] approach, incorporating a more realistic response. The initial assumption for the grain-boundary response [33,34] was ideally plastic with zero work hardening; a second approach [35] used a Voce equation with high work hardening rate. In these early papers, the elastic deformation was assumed to be quasi-isotropic; three types of grains with different (but isotropic) elastic constants, were considered.

Three models are considered here. Model I uses a quasi-isotropic (or "pseudocubic") approach similar to Fu et al. [35]. Within the grains, crystal plasticity (see Section 2) is introduced. Model II incorporates full elastic anisotropy, with the cubic elastic stiffness (C_{11}, C_{12}, and C_{44}). The grain interior is modeled by crystal plasticity, which is more realistic than the isotropic response assumed earlier by Fu et al. [35]. In Model III the mechanical response is assumed to vary continuously. This is done through the change in orientation of the angle of maximum shear stress; the magnitude of the gradient can be incorporated into the work hardening, because it expresses a frequency of cross-slip.

3.1. Model I: Crystal plasticity for grain interiors; Voce equation for grain boundaries

In this model, the grain interiors are assumed to have three orientations. They were modeled with three crystal orientations given by Diehl [45], with an extension (at higher strains) by Suzuki et al. [46]. The grain-boundary regions are governed by a Voce equation with J_2 flow theory, as described in Fu et al. [35]. The two slip directions of the three groups FCC crystals are assumed to be $\phi = \psi = 30°$ (Fig. 2(b)), and the FCC cell has to be rotated according to the specified crystal orientations as shown in Fig. 2(b). The crystal properties for this model and the orientation of the crystals are specified with the simplified two-dimensional assumption. The three orientations considered correspond to the orientations C_{23}, C_{26}, and C_{30} from Diehl [45]. The rotation angles for C_{23} and C_{26} are assumed to be 45° because their locations on crystal stereographic projection positions are close to [1 1 1] and [1 1 0], respectively. For C_{30}, it is assumed to be 90° because it is close to the location of [1 0 0]. The elastic response is assumed to be "pseudocubic" and three sets of Young's moduli are used: E_{23} (for C_{23}), E_{26} (for C_{26}), and E_{30} (for C_{30}). Their values are given in Table 1. They were calculated from the compliance matrix for copper, expressing E_{ijk} according to the standard relationship [47].

The direction cosines are l_1, l_2, and l_3; s_{11}, s_{12}, and s_{44} are the elastic compliances.

Table 1
Parameters for the grain interiors of Model I

Diehl orientation	E (GPa)	v	$\dot{a}$	τ_0 (GPa)	τ_s	h_0
C23	164.3	0.3	0.001	0.1643	$1.8\tau_0$	$8.9\tau_0$
C26	115.2			0.1152	$1.8\tau_0$	$8.9\tau_0$
C30	79			0.079	$1.8\tau_0$	$8.9\tau_0$

$$\frac{1}{E_{ijk}} = s_{11} - 2\left(s_{11} - s_{12} - \frac{1}{2}s_{44}\right)\left(l_1^2 l_2^2 + l_1^2 l_3^2 + l_2^2 l_3^2\right). \tag{10}$$

In this model, the latent hardening effects are not included, and therefore q is set equal to 1; this corresponds to the self-hardening condition.

The grain configuration was established by Voronoi polyhedra [43], as described by Fu et al. [35]. For a grain size $D = 1$ μm, the original configuration is shown in Fig. 3(a). The three colors stand for the three different orientation groups, with the soft C_{30}, medium C_{26}, and hard C_{23} orientations colored red, orange, and yellow–green, respectively. Fig. 3(b)–(c) show the evolution of the von Mises stress distribution in the crystals and Fig. 3(d)–(f) show the equivalent strain distributions. In Fig. 3(b) and (c), the stress rises rapidly, not only in the grain boundary but also inside some of those crystals with harder elastic orientations. The stress is concentrated initially near the central area, as seen in Fig. 3(b). With further compression, all the crystal lattices begin to reorient, and the high stress areas begin to coalesce. Gradually, a shear band is formed, as shown in Fig. 3(c) and (f), and the grain boundaries are subjected to severe

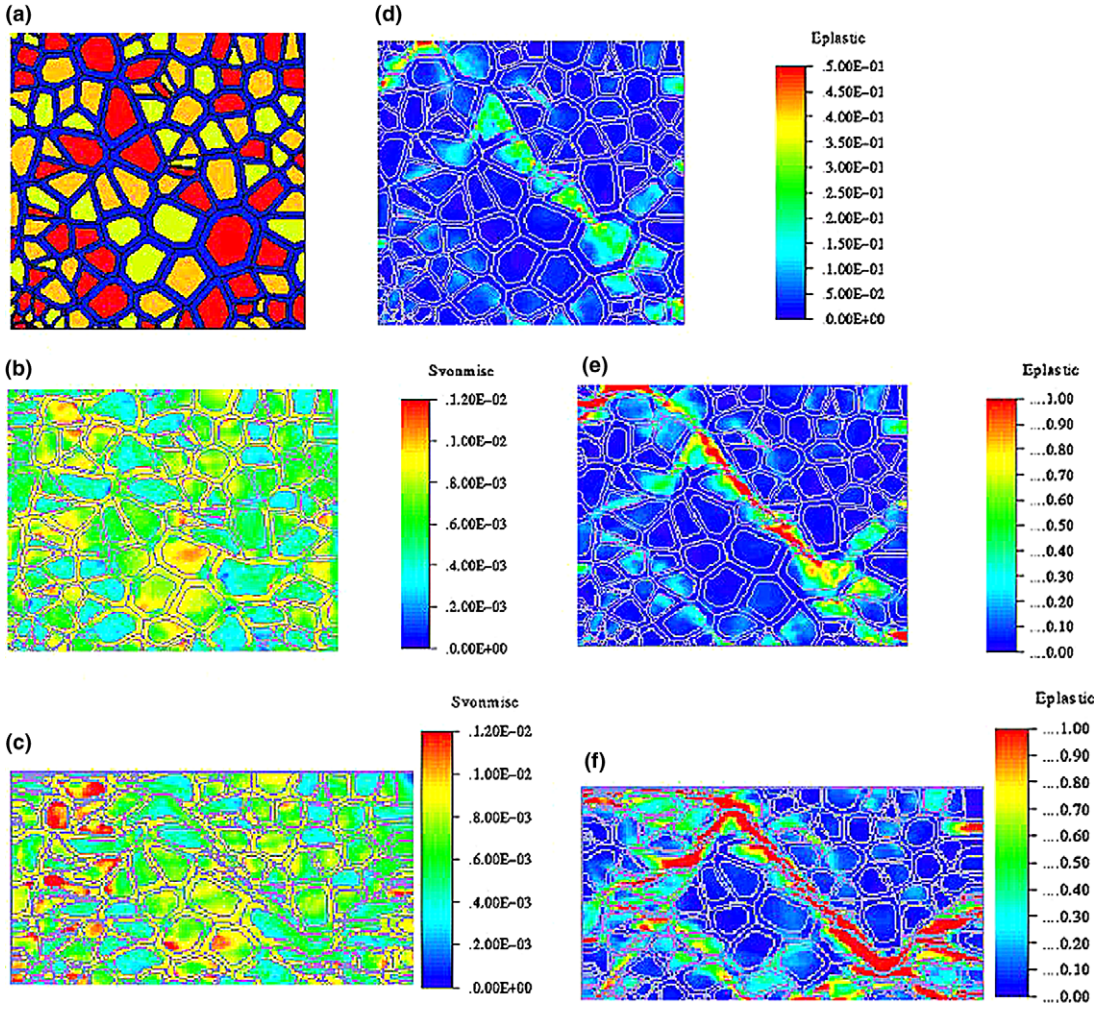

Fig. 3. Compression of polycrystalline copper ($D = 1$ μm): (a) original distribution of three groups of grain interiors (red: C30, orange: C26; yellow–green: C23); (b) and (c) von Mises stress contours for $\bar{\varepsilon}^P = 0.15$ and $\bar{\varepsilon}^P = 0.43$. Equivalent strain contours for [28] (d) $\bar{\varepsilon}^P = 0.047$ (e) $\bar{\varepsilon}^P = 0.15$ (f) $\bar{\varepsilon}^P = 0.43$, where $\bar{\varepsilon}^P$ is the equivalent plastic strain.

shear distortions, resulting in the destruction of the grain boundary structure. This plastic shear flow penetrates through the grain interiors as shown in Fig. 3(c) and (f). In comparison with earlier results of Fu et al. [35], the strain is more localized in Model I; the localization effect is much stronger and the difference between the grains that are located inside and outside of the shear band are larger. The equivalent stress–strain curve is shown in Fig. 4, and the predicted values are about 40% higher than that those obtained earlier by Fu et al. [35]. One possible reason could come from the assumed approximate orientation directions for C_{23}, C_{26}, and C_{30}, since they are not the real tri-dimensional orientations. In conclusion, Model I reveals a more non-uniform failure evolution process in the microstructure, that is closer to microscopic observations.

3.2. Model II: Crystal plasticity for grain boundaries and interior

In this model, both the grain boundaries and grain interiors are modeled with crystal plasticity, and the grain-boundary region surrounding the grain interior has the same orientation as the grain interior. Thus, each boundary region is split into two longitudinally, each half with the same characteristics as the grain in which it is embedded. In Model I, the boundaries were considered a separate region. In contrast to Model I, which uses three orientations, Model II uses fifteen sets of randomly generated, two-dimensional orientation angles. The true elastic anisotropic properties for the cubic symmetry copper are also used, with the material parameters for grain boundaries and grain interiors as given in Table 2.

The reference shear rate is $\dot{a} = 0.001$. In order to model the larger concentration of dislocation sources in the grain boundary, the initial shear strength, τ_0', of the grain boundaries is assumed to be lower than that of grain interior, τ_0. Since the dislocation cross-slip and interactions are more frequent in this region, the saturation shear strength, τ_s, is taken as double that of the grain interior.

Polycrystals with two grain sizes ($D = 1$ μm and $D = 26$ nm) were simulated and compared to experimental results. Fig. 6(a)–(d) shows the evolution of the equivalent plastic strain distributions at the volume averaged equivalent plastic strain $\bar{\varepsilon}^P = 0.0033$, 0.035, 0.1432, 0.4141 for $D = 1$ μm. Fig. 6(e)–(h) shows the corresponding equivalent stress distributions. From Fig. 6(a) and (e), it can be seen that, at the early stages of deformation, the stress in grain boundaries are lower than in the grain interiors while the strain is larger, since the initial shear strength of grain boundaries is assumed to be lower. The higher strain zones distributed along the adjacent grain boundaries join due to the higher stress from the different elastic anisotropies of adjacent crystals. It then forms a network structure of grain boundaries. From Fig. 6(b), it is seen that the localized strain zone continues to grow and the grain interiors surrounded by these grain boundaries start to work harden. The strain inside these grains increases, espe-

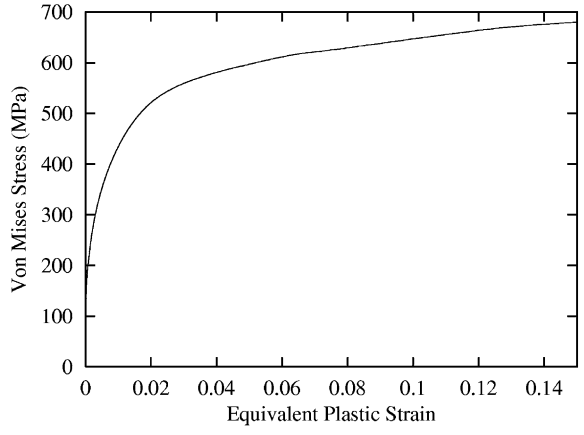

Fig. 4. Computed stress–strain curve for Model I ($D = 1$ μm).

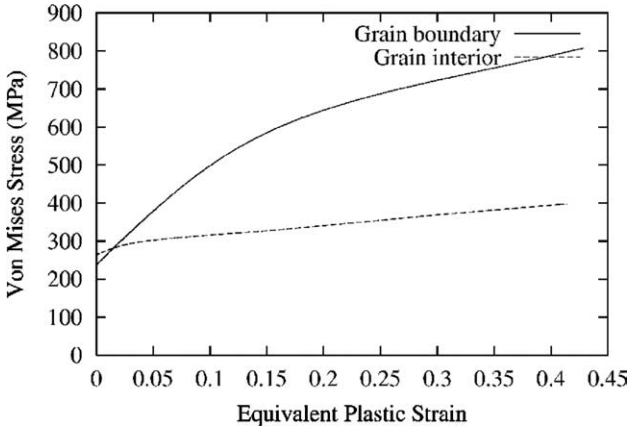

Fig. 5. Mechanical response for grain interior and grain boundary for Model II.

Table 2
Parameters for the grain interiors and grain boundaries of Model II

	Elastic constants (GPa)			Plastic constants (GPa)		
	C_{11}	C_{44}	C_{12}	τ_0, τ_0'	τ_s	h_0
Grain interior	168.4	75.4	121.4	0.168	0.1848	0.336
Grain boundary	168.4	75.4	121.4	0.1512	0.3628	1.0584

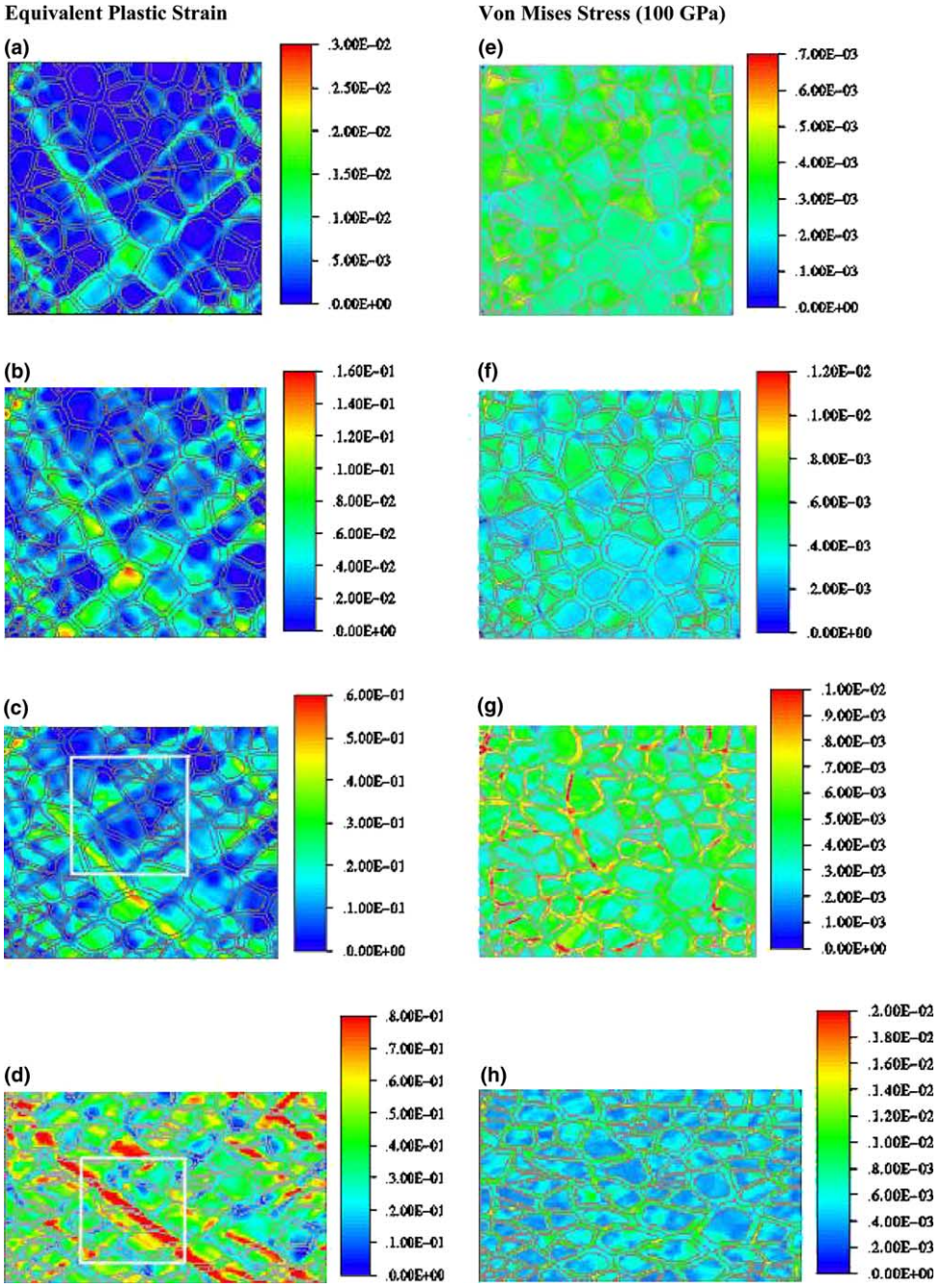

Fig. 6. Compression of polycrystalline copper ($D = 1$ μm) Model II, right column shows equivalent strain: (a) $\bar{\varepsilon}^{P} = 0.0033$; (b) 0.035; (c) 0.1432; (d) 0.4141, left column; (e)–(h) shows the corresponding von Mises stresses; colors describe stress and strain levels.

cially at the triple point junctions of the grain boundaries. In Fig. 6(f), regions with low stresses have high levels of plastic strain, and vice versa, due to the differences in the stress–strain relations between the crystals and their boundaries. As the compression continues, Fig. 6(c) shows the region of peak strain (red area), in Fig. 6(b), which begins to slide, and coalesces with other regions of large strains to form a shear band along the grain boundaries. Finally, in Fig. 6(d), several strong shear bands are formed. Fig. 7 shows close-ups at effective strains $\bar{\varepsilon}^{P} = 0.1432$ and $\bar{\varepsilon}^{P} = 0.4141$. The initiation and propagation of localization can be seen. It should be noted that this localization occurs concurrently with hardening.

For the $D = 26$ nm case, the material is composed mainly of grain boundary. Based on the aforementioned weaker initial shear strength assumption, the initial strain localization occurs in the grain boundaries as shown in Fig. 8(a), especially near the intersections among different crystals. Fig. 8(a)–(d) have the same

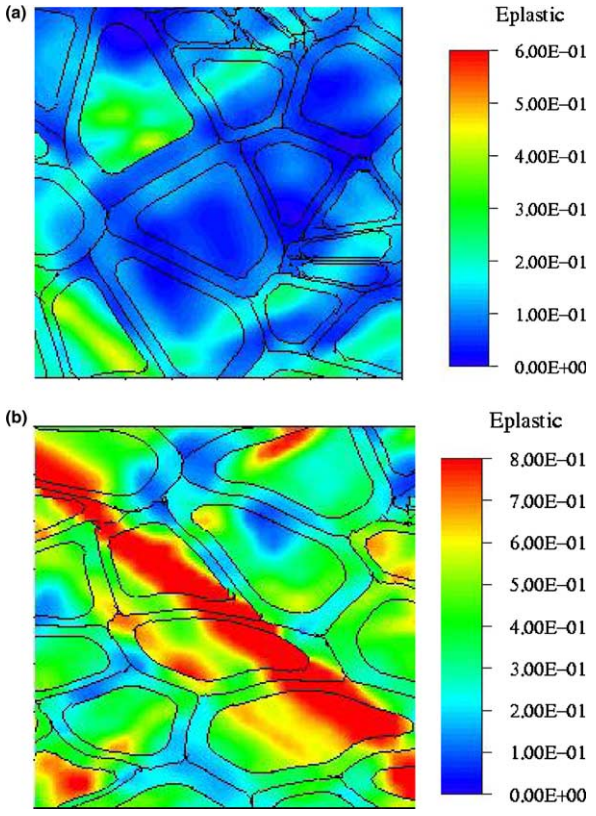

Fig. 7. Close-up (marked boxes in Fig. 5), showing detail of plastic deformation for two imposed strains: (a) $\bar{\varepsilon}^{\mathrm{P}} = 0.1432$; (b) $\bar{\varepsilon}^{\mathrm{P}} = 0.4141$.

strains as in Fig. 6(a)–(d). It is apparent in Fig. 8(b) that the strain localization is not as strong in the grain interior as in the $D = 1$ μm case due to the larger amount of rapidly work hardening grain boundary structures, which sustain and distribute the compression loading. In Fig. 8(c) and (d), the localized regions gradually join and regions of localized strain appear in the matrix where the stress is clearly concentrated. In Fig. 8(d), shear band is formed and it passes by, or through, a series of softer grain interiors. By comparing the scaled contour plot of Fig. 6(d) and Fig. 8(d), it can be seen that the final localized shear band often penetrates through the boundaries between the grain interiors and grain boundaries, and therefore, areas where there is a discontinuity of mechanical properties are the weakest part of the whole material. Fig. 9 shows a close-up of the shear localization region in Fig. 8(d).

The crystal orientation of $D = 26$ nm for the initial state and final state are shown in Fig. 10(a) and (b). Among these crystals, the misorientation of the material can be clearly seen, especially near the grain boundary joints or the triple points. This material misorientation is a cause of geometric softening [40], and thus there should be a higher stress concentration in these regions (just like in the plate tension case), which is in good agreement with Meyers and Ashworth [32]. The equivalent stress–strain curves of $D = 1$ μm and $D = 26$ nm cases are shown in Fig. 11, and the case of $D = 26$ nm shows a higher work hardening rate and a stiffer response. Nevertheless, the difference between these two curves is smaller than the difference calculated by Fu et al. [35].

3.3. Model III: Continuously varying mechanical response

A different approach was implemented in the establishment of the grain-boundary effect. It provides a continuous change in hardening as a function of position within the polycrystalline aggregate. One of the ways in which continuum hardening can be related to discrete dislocation processes happening inside the material is by tracking the change in the direction of maximum shear stress. If this direction changes, it will trigger cross-slip and increased hardening, as shown schematically in Fig. 1. The angle ϕ, corresponding to this direction, is given by

$$\tan 2\phi = \frac{(\sigma_x - \sigma_y)}{2\tau_{xy}}, \tag{11}$$

where $\sigma_x, \sigma_y, \tau_{xy}$ are the two-dimensional stresses. The gradient of this direction is equal to

$$\nabla\phi = \frac{\partial\phi}{\partial x}\vec{\mathrm{i}} + \frac{\partial\phi}{\partial y}\vec{\mathrm{j}}. \tag{12}$$

The square of the magnitude of this gradient is

$$\nabla\phi^2 = \left(\frac{\partial\phi}{\partial x}\right)^2 + \left(\frac{\partial\phi}{\partial y}\right)^2. \tag{13}$$

Fig. 12 shows the distribution of this parameter within a few grains in a polycrystal at an imposed strain. There are two color scales on figure: the one in the left applies to $D = 1$ um, while the one in the right applies to $D = 26$ nm. The gradients are much larger for the small grain size by virtue of the reduced length scale. The magnitude of $\nabla\phi$ is clearly connected to grain boundaries. It also varies throughout the polycrystal in a continuous manner. The interiors of the grains are primarily blue (zero value of gradient). This denotes a constancy in the direction of maximum shear.

In order to obtain a local stress–strain relationship from the physical processes alluded to above, one has to assume that the material has a local yield stress and work hardening rates that are a function of the distance from the grain boundary. The yield stress can be expressed, as a function of distance l from the closest grain boundary ($l \geqslant b$, the Burgers vector), as

$$\tau_0 = \tau_0' + (\tau_0 - \tau_0')\left(1 - \frac{1}{l/b}\right). \tag{14}$$

τ_0 and τ_0', as defined in Section 3.2, are the yield stress of the grain interior and grain boundary, respectively.

The work hardening term may be introduced through the Seeger Stage II [48–50] work hardening

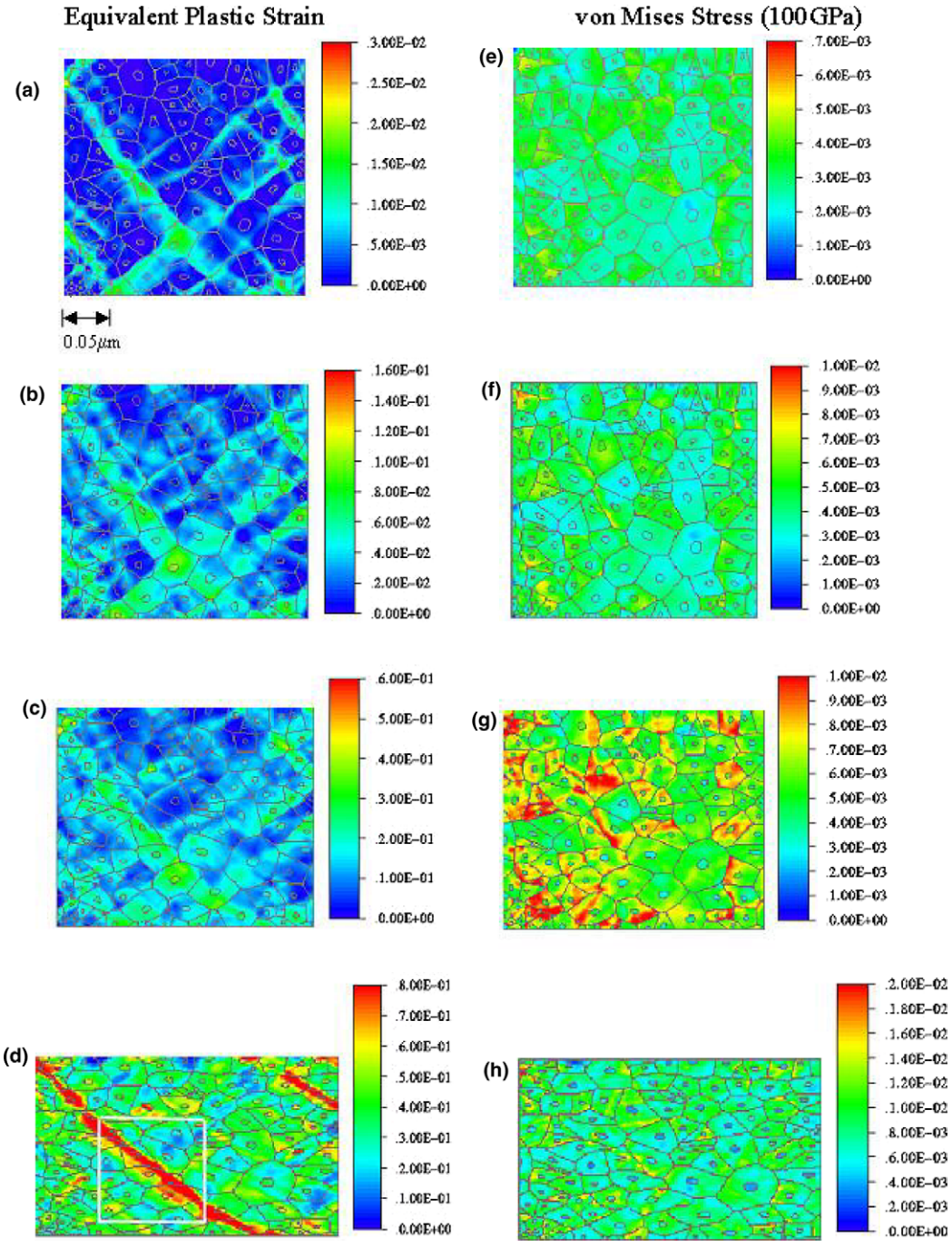

Fig. 8. Compression of polycrystalline copper ($D = 26$ nm, Model II), left column shows equivalent strains: (a) $\bar{\varepsilon}^{P} = 0.0033$; (b) 0.035; (c) 0.1432; (d) 0.4141; right column (e)–(h) shows the corresponding von Mises stresses, colors describe stress and strain levels.

theory. This is not a unique approach, but it is simple and suffices for the purpose of the work presented herein. Seeger [48–52] assumes that most of slip in Stage II still takes place on the primary plane. He defines a length L which is the distance between blocks from secondary slip activity. Seeger [49,50] found that the barrier spacing was inversely proportional to Stage II strain. This distance, L, is reduced with strain, γ, as

$$L = \frac{\Lambda}{\gamma - \gamma^*}. \tag{15}$$

γ^* is the shear strain at the onset of Stage II hardening. The observed value for the proportionality constant was $\Lambda \approx 4 \times 10^{-6}$ m. We modify the above expression by incorporating the magnitude of the gradient, since the cross-slip activity is dependent on the change in orientation of the plane of maximum shear. We also eliminate

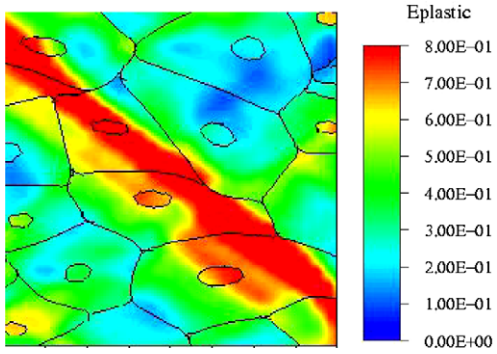

Fig. 9. Close-up (marked box in Fig. 8) showing details of plastic deformation for $\bar{\varepsilon}^{P} = 0.4141$; notice shear localization.

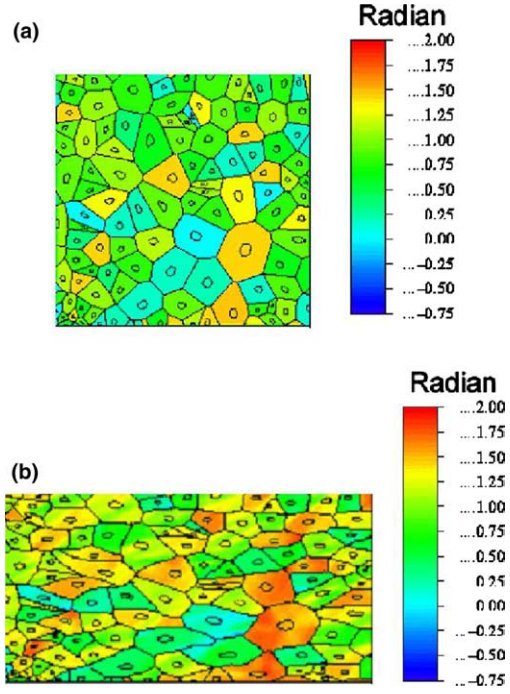

Fig. 10. Change in crystal orientations for $D = 26$ nm (Model II): (a) initial orientations; (b) final crystal orientations ($\bar{\varepsilon}^{P} = 0.41$).

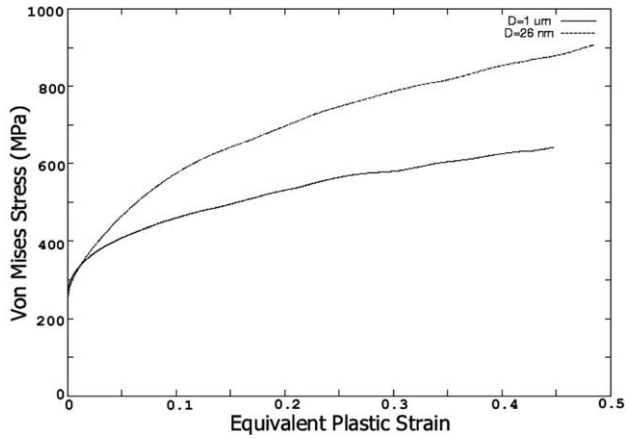

Fig. 11. Equivalent stress–strain curves for $D = 1$ μm and $D = 26$ nm (Model II).

γ^{*} and assume Stage II from the onset of plastic deformation.

$$L = \frac{\Lambda'}{\gamma|\nabla\phi|}. \tag{16}$$

The parameter Λ' has dimensions of rd. The increment of strain, $\mathrm{d}\gamma$, is obtained by Seeger from an expression analogous to the Orowan equation; a critical difference is that the strain increment is related to an increase in dislocation density, and not to an increase in distance traveled by each dislocation. Seeger et al. [49] assumed rectangular loops. For simplicity, we assume square loops with side L. Thus

$$\mathrm{d}\gamma = bL^{2}\,\mathrm{d}N. \tag{17}$$

The dislocation density is LN. The athermal component of shear stress, τ_G, is related to the dislocation density by the well known expression

$$\tau_G = \alpha_1 bG(NL)^{1/2}. \tag{18}$$

α_1 is a parameter in the Seeger derivation [49]. It is related to n, the number of dislocation piled up in front of each barrier produced by secondary slip, by

$$\alpha_1 = 0.2n^{1/2}.$$

Seeger et al. [49] estimate that $\alpha_1 = 0.2$. The work hardening is obtained by taking the derivative of Eq. (18) with respect to γ:

$$\frac{\mathrm{d}\tau_G}{\mathrm{d}\gamma} = \frac{\alpha_1 bG}{2}\left[\left(\frac{L}{N}\right)^{1/2}\frac{\mathrm{d}N}{\mathrm{d}\gamma} + \left(\frac{N}{L}\right)^{1/2}\frac{\mathrm{d}L}{\mathrm{d}\gamma}\right]. \tag{19}$$

From Eq. (16) one has

$$\frac{\mathrm{d}L}{\mathrm{d}\gamma} = \frac{-\Lambda'}{|\nabla\phi|}\gamma^{-2}. \tag{20}$$

From Eq. (17) one has

$$\frac{\mathrm{d}N}{\mathrm{d}\gamma} = \frac{1}{bL^{2}}. \tag{21}$$

Substituting Eqs. (20) and (21) into (19) eventually leads to

$$\frac{\mathrm{d}\tau_G}{\mathrm{d}\gamma} = \frac{\alpha_1^{2}G^{2}b}{2\Lambda'\tau_G}\gamma|\nabla\phi| + \frac{b}{2}\tau_G\frac{\Lambda'}{\gamma|\nabla\phi|}. \tag{22}$$

By assuming that $|\nabla\phi|$ is constant and dependent on position only, we have the following differential equation:

$$\frac{\mathrm{d}\tau_G}{\mathrm{d}\gamma} = \frac{A}{\gamma}\tau_G + B\gamma\tau_G^{-1}, \tag{23}$$

where

$$A = \frac{b\Lambda'}{2|\nabla\phi|}, \tag{24}$$

$$B = \frac{\alpha_1^{2}G^{2}}{2\Lambda'}b|\nabla\phi|. \tag{25}$$

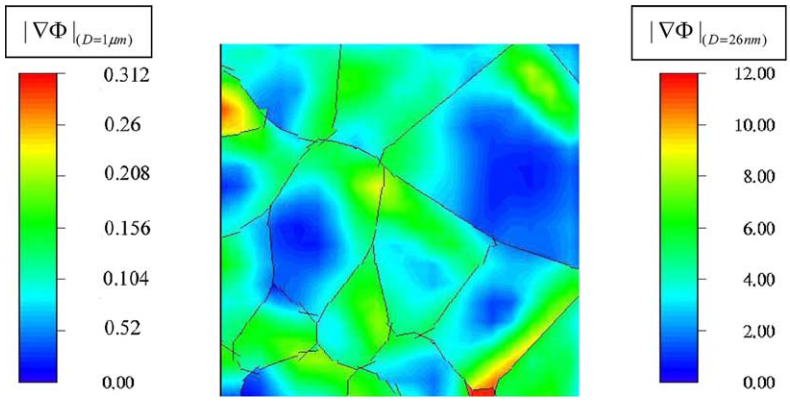

Fig. 12. Distribution of magnitude of gradient of angle of maximum shear stress throughout polycrystalline aggregate. Left-hand scale: $D = 1$ μm; right-hand scale: $D = 26$ nm.

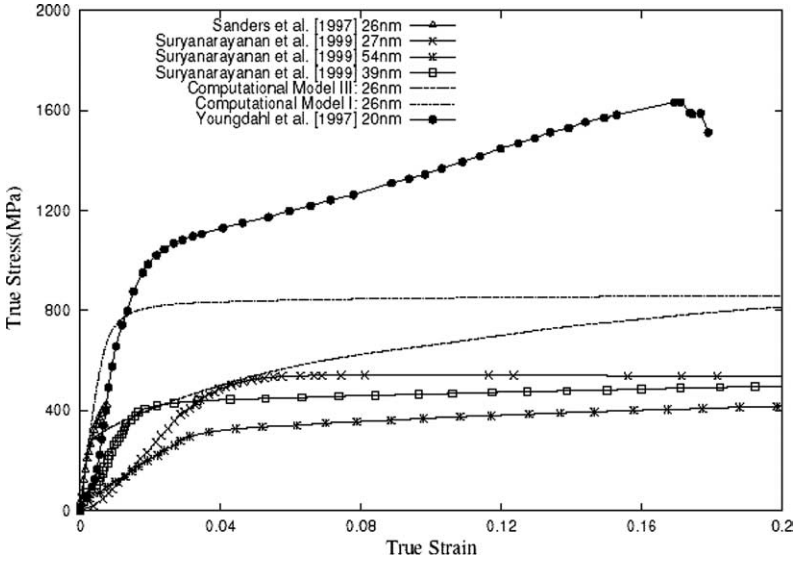

Fig. 13. Computed results compared to experiments for grain sizes in nanocrystal range; notice wide range of experimental results.

The general solution is

$$\tau_G^2 = \frac{C_1 B\gamma^2}{1-A} + C_2\gamma^{2A}. \tag{26}$$

From Eq. (26), the local flow stress can be obtained as a function of strain if the constants C_1 and C_2 are found.

We can add a term that takes into account the flow stress dependence on position within the grain (Eq. (14)). The modified equation is

$$\tau_G = \tau_0' + (\tau_0 - \tau_0')\left(1 - \frac{1}{l/b}\right) + \left(\frac{C_1 B\gamma^2}{1-A} + C_2\gamma^{2A}\right)^{1/2}. \tag{27}$$

Eq. (27) enables the determination of the local flow stress as a function of imposed shear strain and position within the grain. It provides a continuous variation in work hardening.

3.4. Additional considerations

3.4.1. Comparison with experimental results

In this study, with the phenomenological model, the simulations were conducted for grain sizes of 26 nm and 1 μm. This is for comparison purposes with experimental results in the grain-size range 20–54 nm reported in the literature [53–57]. The computational procedures and results are presented in Section 3. In this section the computational results of Fu et al. [35] and Model II of $D = 26$ nm are plotted to compare with recent experimental measurements. The experimental measurements have a large variation as shown in Fig. 13. It can be seen that for $D = 26$ nm the computational model by Fu et al. [35] predicts faster work hardening as compared to Model II. Model II reveals a slower initial work hardening rate and the hardening process is much longer.

At small strains Model II agrees with the Sanders et al. curve [57], but its initial yield point is too low, and in the middle stage it runs close to the results of Suryanarayanan [54,55] ($D = 27$ nm) and continues to work harden. For the current work, both Model I and Model II can successfully simulate the strengthening phenomena of nanocrystalline copper, and they provide a useful way to study the evolution of microstructure for polycrystalline copper. The great spread in the experimental results is a clear demonstration that the accuracy of calculations cannot, at the present moment, be checked against results.

3.4.2. Shear localization

Both Models I and II exhibit shear localization. Figs. 8 and 9 show the evolution of the process: a well-defined shear band is formed at $\bar{\varepsilon}^{P} = 0.4$. This shear localization is indeed a dominant deformation mechanism in nanocrystalline materials. Ma [59] observed localization in and nanocrystalline copper, and Wei et al. [60] and Jia et al. [61] observed the same phenomenon in ultrafine grained iron. The reason for this is the virtual absence of work hardening in these materials, after a few per cent of plastic deformation. The grain boundaries are the primary sources and sinks of dislocations, and their mean free path is so small that little interaction (cross slip, reactions, etc.) exists. The observations by TEM [59–61] reveal enlarged grains within the shear localization regions. These grains are elongated in the shear direction and are thought to provide paths for dislocations.

These complex changes cannot, at present, be incorporated into the model presented herein. Nevertheless, the agreement between computations and experimental observations is considered more than fortuitous. Localization takes place concurrently with hardening in the computations. This could well represent the initiation of the process. The material within this region is subjected to drastic reorientation that would then lead to the creation of favored paths for dislocation motion. The elongated grains would provide the larger mean free paths for these dislocations.

3.4.3. Grain-boundary sliding

The negative Hall–Petch slope obtained experimentally by Chokshi et al. [58] has been at the center of considerable debate. The picture that is emerging is that, for grain sizes on the order of 20 nm and lower, sliding becomes an important deformation mechanism and lowers the yield stress. Fu et al. [35] included grain-boundary sliding and diffusional accommodation through a sinusoidal Raj–Ashby [62] boundary and showed that, for $d \leqslant 10$ nm, this effect was important. Recently, Conrad and Narayan [63,64] carried out experiments showing the inverse Hall–Petch relationship. Conrad [65] developed a model that predicts the inverse relationship. In the current calculations the smallest grain size was 26 nm. Thus, there is no need to incorporate this effect (cf. Fig. 10).

4. Conclusions

Three computational models are proposed to predict the effect of grain size and microstructural evolution, while retaining the single crystal response within the grain interiors:

1. Model I uses crystal plasticity in the grain interior and a Voce equation in the grain boundaries. Elastic anisotropy is accounted for by considering three orientations with different Young moduli, calculated from the anisotropic elastic compliances. Its mechanical response is somewhat too stiff, and the isotropic plasticity in the grain boundaries result in unrealistic deformation.
2. Model II is a more realistic model because it uses crystal plasticity for both the grain interiors and grain boundaries. Elastic anisotropy is fully accounted for by the use of the elastic stiffness matrix for copper. Although in this study, the calculated mechanical response does not exhibit a grain size dependence as strong as that observed in experiments, it does provide a good simulation of the evolution of shear localization in the microstructures. This localization occurs with global hardening. The calculations also show more detail in the crystal slip phenomenon.
3. Model III uses a novel approach. A continuous change in work hardening is introduced. This hardening is related to the dislocation density evolution, which is dictated by cross-slip frequency. One parameter that governs this evolution is the change in orientation of the plane of maximum shear stress; the magnitude of the gradient of the maximum shear stress angle is used here. Computations using this parameter demonstrate that the grain-boundary regions are indeed subjected to accelerated hardening.

The computational models successfully predict the grain size effects and provide valuable information about the deformation evolution. It is shown that the variation among experimental results in the nanocrystalline range by different investigators is considerable and therefore the fine-tuning of models cannot be carried out at the current stage. The evolution of this polycrystalline/nanocrystalline model has proceeded by first assuming a perfectly plastic grain-boundary region [34] to one hardening at higher rate than the grain interior [35]; in the effort presented here, crystal plasticity with texture evolution has been introduced first in a core and mantle scheme, than in a physically based continuous variation of mechanical response, see Fig. 11. Recent observations show the formation of a grain-boundary work hardened layer [66].

Acknowledgements

This research was supported by the US Army Research Office Multidisciplinary University Research Initiative (Contract No. DAAH 04-96-1-0376), NSF Grants DMI-9612017 and CMS-0210173 (NIRT). Prof. V. Lubarda provided many valuable insights. Discussions with Prof. R.J. Asaro and Dr. B.K. Kad are gratefully acknowledged. Miss B.Y. Cao's help in the last stages of manuscript preparation are appreciated.

References

[1] Gleiter H. Acta Mater 2000;48:1.
[2] Kumar KS, Van Swygenhofen H, Suresh S. Acta Mater 2003;51:5743.
[3] Taylor GI, Elam CF. Proc R Soc London 1925;28:102.
[4] Taylor GI. Proc R Soc London 1938:307.
[5] Bishop JFW, Hill JFW. Philos Mag 1951;42:414.
[6] Bishop JFW. J Mech Phys Solids 1954;3:130.
[7] Dillamore IL, Kaoth H. Met Sci 1974;8:21.
[8] Hill R, Rice JR. J Mech Phys Solids 1972;20:401.
[9] Asaro RJ, Rice JR. J Mech Phys Solids 1977;25:309.
[10] Kröner E, Teodosiu C. In: Proc of the Symposium on Foundation of Plasticity Nordhoff International Pub. Leyden, p. 93.
[11] Budiansky B, Wu TY. In: Proc of the 4th US Nat Cong APPL Mech, 1962, p. 1175.
[12] Berveiller M, Zaoui AJ. Mech Phys Solids 1979;26:325.
[13] Molinari A, Canova GR, Ahzi S. Acta Metall 1987;35:2983.
[14] Canova G, Fresseangeas C, Molinari A, Kocks UF. Acta Metall 1988;36:1961.
[15] Lubarda V. Elastoplasticity theory. Boca-Raton (FL): CRC Press; 2002.
[16] Lin G, Havner KS. Int J Plast 1994;10:471.
[17] Anand L, Kalidindi SR. Mech Mater 1994;17:223.
[18] Kocks UF, Tomé CN, Wenck H-R. Texture and anisotropy: preferred orientations in polycrystals and their effects on materials properties. Cambridge: Cambridge Uniuersity Press; 1998.
[19] Peirce D, Asaro RJ, Needleman A. Acta Metall 1982;30:1087.
[20] Peirce D, Asaro RJ, Needleman A. Acta Metall 1983;31:1951.
[21] Harren SV, Asaro RJ. J Mech Phys Solids 1988;37:191.
[22] Marin EB, Dawson PR. Comput Methods Appl Mech Eng 1996;165:23.
[23] Mika DP, Dawson PR. Acta Mater 1999;47:1355.
[24] Barbe F, Decker L, Jeulin D, Cailletaud G. Int J Plast 2000;17:513.
[25] Armstrong RW. In: Bunshah RF, editor, Advances in materials research, vol. 5. New York: Interscience; 1971. p. 101.
[26] Ashby MF. Philos Mag 1970;21:399.
[27] Yao Z, Wagoner RH. Acta Metall Mater 1993;41:451.
[28] Suits JC, Chalmers B. Acta Metall 1961;9:854.
[29] Worthington PJ, Smith E. Acta Metall 1966;15:1277.
[30] Hook RE, Hirth JP. Acta Metall 1967;15:535.
[31] Delaire F, Rafanel JL, Rey C. Acta Mater 2000;48:1075.
[32] Meyers MA, Ashworth E. Philos Mag 1982;46:737.
[33] Meyers MA, Benson DJ, Fu H-H. In: Chung Y-W, Dunand DC, Liaw PK, Olson, GB, editors, Advanced materials for the 21st Century. Warrendale (PA): TMS-AIME; 1999. p. 499–512.
[34] Benson DJ, Fu H-H, Meyers MA. Mater Sci Eng A 2001;319:854.
[35] Fu H-H, Benson DJ, Meyers MA. Acta Mater 2001;49:2567.
[36] Kim HS, Estrin Y, Bush MB. Mater Sci Eng A 2001;316:195.
[37] Estrin Y, Sluys B, Brechet Y, Molinari A. J Phys IV 1998;8(P8):135.
[38] Van Swygenhofen H, Caro A. Phys Rev B 1998;58:11246.
[39] Van Swygenhofen H, Spaczer M, Caro A. Acta Mater 1999;47:3117.
[40] Lee EH, Liu DT. J Appl Mech 1967;38:19.
[41] Anand L. In: Meyers MA, Armstrong RW, Kirchner HOK, editors. Mechanics and materials fundamentals and linkages. New York: Wiley–Interscience; 1999. p. 231.
[42] Hutchinson JW. Proc R Soc London A 1970;319:247.
[43] Voronoi GZ. Reine Angew Math 1908;1345:199.
[44] Kocks UF, Mecking H. Prog Mater Sci 2003;48:171.
[45] Diehl J. Z Metallkd 1956;47:331.
[46] Suzuki H, Ikeda T, Tanaka T. J Phys Soc Jpn 1956;1:382.
[47] Nye JF. Physical properties of crystals. Clarenden Press: Oxford University; 1957. p. 145.
[48] Seeger A, Mader S, Kronmuller H. In: Thomas G, Washburn J, editors. Electron microscopy and strength of crystals. New York: Wiley–Interscience; 1963. p. 665.
[49] Seeger A, Diehl J, Madrer S, Rebstock H. Philos Mag 1957;8:323.
[50] Mader S, Seeger A, Leitz C. J Appl Phys 1963;34:3368.
[51] Mader S, Seeger A, Thieringen HM. J Appl Phys 1963;34:3376.
[52] Seeger A. In: Dislocations and mechanical properties of crystals. New York: Wiley; 1957. p. 243.
[53] Weertman JR. Mater Sci Eng A 1993;166:161.
[54] Suryanarayana C, Fores FH. Met Trans A 1992;23:1071.
[55] Suryanarayana C, Koch CC. Hyperfine Interact 2000;130:5–44.
[56] Youngdahl CJ, Sanders PG, Eastman JA, Weertman JR. Scr Mater 1997;37:811.
[57] Sanders PG, Eastman JA, Weertman JR. Acta Mater 1997;45:4023.
[58] Chokshi AH, Rosen A, Karch J, Gleiter H. Scr Metall 1989;23:1679.
[59] Ma E. Scr Mater 2002;49:663.
[60] Wei Q, Jia D, Ramesh KT, Ma E. Appl Phys Lett 2002;81:1240.
[61] Jia D, Ramesh KT, Ma E. Acta Mater 2003;51:3495.
[62] Raj R, Ashby MF. Met Trans 1971;2:1113.
[63] Conrad H, Narayan J. Scr Mater 2000;42:1025.
[64] Conrad H, Narayan J. Acta Mater 2002;50:5067.
[65] Conrad H. Met Mat Trans 2004.
[66] Gray III GT, Chen SR, Vecchio KS. Met Mat Trans 1999;30A:1235.